Check for updates

A continuous flow diffusion chamber study of sea salt particles acting as cloud nuclei: deliquescence and ice nucleation

By XIANGRUI KONG[1,2*], MARTIN J. WOLF[1], MICHAEL ROESCH[1], ERIK S. THOMSON[2], THORSTEN BARTELS-RAUSCH[3], PETER A. ALPERT[3], MARKUS AMMANN[3], NØNNE L. PRISLE[4] and DANIEL J. CZICZO[1,5*], [1]*Earth, Atmospheric and Planetary Sciences, Massachusetts Institute of Technology, Cambridge, MA, USA;* [2]*Department of Chemistry and Molecular Biology, University of Gothenburg, Gothenburg, Sweden;* [3]*Laboratory of Environmental Chemistry, Paul Scherrer Institute, Villigen, Switzerland;* [4]*Nano and Molecular Systems Research Unit, University of Oulu, Oulu, Finland;* [5]*Civil and Environmental Engineering, Massachusetts Institute of Technology, Cambridge, MA, USA*

ABSTRACT

Phase changes of sea salt particles alter their physical and chemical properties, which is significant for Earth's chemistry and energy budget. In this study, a continuous flow diffusion chamber is used to investigate deliquescence, homogeneous and heterogeneous ice nucleation between 242 K and 215 K, of four salts: pure NaCl, pure $MgCl_2$, synthetic sea water salt, and salt distilled from sampled sea water. Anhydrous particles, aqueous droplets and ice particles were discriminated using a polarisation-sensitive optical particle counter coupled with a machine learning analysis technique. The measured onset deliquescence relative humidities agree with previous studies, where sea water salts deliquescence at lower humidities than pure NaCl. Deliquesced salt droplets homogenously freeze when the relative humidity reaches a sufficiently high value at temperatures below 233 K. From 224 K and below, deposition nucleation freezing on a fraction of NaCl particles was observed at humidities lower than the deliquescence relative humidity. At these low temperatures, otherwise unactivated salt particles deliquesced at the expected deliquescence point, followed by homogeneous freezing at temperatures as low as 215 K. Thus, the observed sea salt particles exhibit a triad of temperature-dependent behaviours. First, they act as cloud condensation particles (CCNs) > 233 K, second they can be homogeneous freezing nuclei (HFNs) < 233 K and finally they act as ice nucleating particles (INPs) for heterogeneous nucleation <224 K.

Keywords: sea salt, deliquescence, homogeneous ice nucleation, heterogeneous ice nucleation, continuous flow diffusion chamber

1. Introduction

Sea salt particles are abundant in the atmosphere (O'Dowd et al., 1997), important to the terrestrial radiation budget, act as cloud nuclei and participate in heterogeneous halogen chemistry (Abbatt et al., 2012; Gantt and Meskhidze, 2013). Originating from sea spray, sea salt particles can be transported from the open sea to be deposited on land or snow cover (Domine et al., 2004) where they can be modified and again become airborne particles due to wind action (Yang et al., 2008; Huang and Jaegle, 2017). As the predominant component of sea salt, NaCl exhibits many of the main features of sea salts. For

example, sea salt particles take up water close to the deliquescence relative humidity (DRH) of pure NaCl (Martin, 2000; Wise et al., 2009), ~75% at 293 K (Tang and Munkelwitz, 1993), which makes sea salt particles efficient cloud condensation nuclei (CCNs). At low temperatures, sea salt particles/droplets can act as either homogeneous freezing nuclei (HFNs) or ice nucleating particles (INPs), depending on whether deliquescence overcomes ice nucleation or *vice versa* (Wise et al., 2012). Sea salt particles have also been observed to contribute to cirrus cloud formation, especially over open oceans where deep convection is present, to loft particles from the surface, high into the atmosphere (Cziczo et al., 2004; Twohy and Poellot, 2005; Cziczo et al., 2013).

---

*Corresponding author. e-mail: kongx@chem.gu.se (Xiangrui Kong); djcziczo@mit.edu (Dan Cziczo)

1

The phase changes of the binary NaCl–water system have been extensively studied (Koop et al., 2000a; Křepelová et al., 2010; Yang et al., 2017). Using a single particle levitation set-up, Tang et al. measured and parameterised the DRH and efflorescence RH (ERH) of NaCl and multicomponent particles at temperatures above 273 K, where DRH was found to have a slightly negative temperature dependence (Tang and Munkelwitz, 1993). At lower temperatures, Wise et al. (2012) and Koop et al. (2000a) both observed that NaCl crystals deliquesce to form supercooled solution at temperatures down to 233 K, in good agreement with the extrapolation of the Tang parameterisation (Tang and Munkelwitz, 1993). Observations of airborne salt particles between 228 and 233 K in a large aerosol and cloud (Aerosol Interaction and Dynamics in the Atmosphere, AIDA) chamber showed similar phase behaviour (Wagner and Möhler, 2013). Sea salts with more complex composition were found to have lower DRHs and lower growth factors than those of NaCl (Ming and Russell, 2001; Alshawa et al., 2009; Wise et al., 2009; Cochran et al., 2017). The altered hygroscopicity is attributed to inorganic materials with lower DRHs than NaCl (Kester et al., 1967; Cziczo et al., 1997) and the presence of organics (O'Dowd et al., 2004; Alshawa et al., 2009; Wise et al., 2009; Schill and Tolbert, 2014; Ladino et al., 2016).

In the atmosphere, deliquesced solution droplets freeze homogeneously when the critical temperatures corresponding to the water activity are met (Koop et al., 2000b), something which has been observed in both laboratories and field measurements (Koop et al., 2000a; Alpert et al., 2011; Ladino et al., 2016). After deliquescence, if an insoluble surface remains in contact with the saturated solution, deliquescent heterogeneous freezing (DHF) may occur (Khvorostyanov and Curry, 2004). Deposition nucleation of ice *vis-á-vis* water vapour deposition directly onto anhydrous NaCl particles, can occur at low temperatures when the saturation vapour pressure is less than the DRH (Wise et al., 2012; Schill and Tolbert, 2014). This competition between freezing and deliquescence is complicated and not yet well resolved at low temperatures (Khvorostyanov and Curry, 2004; Petzold et al., 2013). Complicating matters further, the presence of organics at particle surfaces could prevent deposition nucleation, leading to deliquescence followed by homogeneous ice nucleation (Ladino et al., 2016). The NaCl–water system also contains a dihydrate (NaCl·2H$_2$O) that forms at temperatures below 252 K, and has been recognised to make efficient INPs (Wise et al., 2012; Wagner and Möhler, 2013).

The low-temperature continuous flow diffusion chamber (CFDC), which exposes particles to controlled temperature and humidity conditions, is a powerful tool for investigating ice nucleation (Hussain and Saunders, 1984; Rogers, 1988). When equipped with suitable optical detectors, CFDCs can discriminate different phases of particles using size and polarisation information (Garimella et al., 2016). Despite the capabilities of CFDCs, this type of instrument has not been previously used to determine aerosol phase transitions beyond ice nucleation.
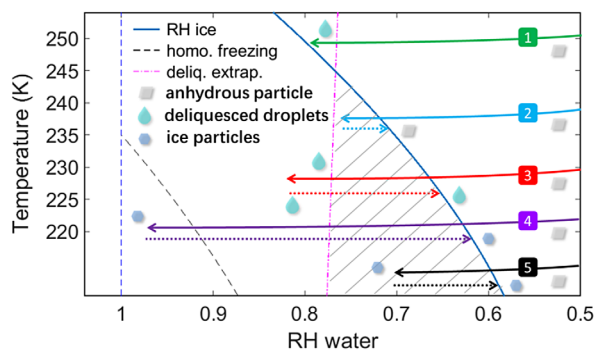

Fig. 1. NaCl–water phase diagram in temperature-RH$_w$ space. The blue solid curve represents ice saturation (Johari et al., 1994; Koop et al., 2000b) and the pink dash-dotted line represents the DRH extrapolated from measurements at higher temperatures (>278 K) (Tang and Munkelwitz, 1993). Notes: The black dashed line is the homogeneous freezing line from Koop et al. (2000a), for droplets between 1 and 10 μm. The solid and dotted lines 1-5 correspond to experimental trajectories, where the solid portions depict the experimental exposure entering the CFDC main chamber and dashed portions represent the return to ice saturation that occurs within the evaporation section of the CFDC.

To illuminate the potential of low-temperature CFDC studies, we consider the NaCl–water phase diagram at low temperatures and overlay possible experimental trajectories (Fig. 1, solid numbered lines). In the figure the blue curve illustrates ice saturation, which is the lowest possible RH$_w$ that can be achieved with an ice-coated wall CFDC, such as the spectrometer for ice nuclei (SPIN) used for this study (Garimella et al., 2016).

At temperatures above ~245 K, the lowest RH$_w$ in the CFDC, ice saturation, is always higher than the DRH, and therefore it is not feasible to prevent anhydrous NaCl particles from deliquescing within the chamber (green trajectory 1). However, below ~245 K, anhydrous NaCl may remain between the DRH and ice saturation (shown as the shaded area) until exiting the chamber (blue trajectory 2). If the chamber RH$_w$ exceeds the DRH, the anhydrous salt will be expected to deliquesce (red trajectory 3) and the droplets are expected to remain aqueous even at RH$_w$ < DRH in an evaporation section at the bottom of the CFDC (see section 2.2 and (Garimella et al., 2016)). This is a result of the hysteresis between deliquescence and efflorescence that results in a metastable gap of RH$_w$ (DRH ~65% > ERH ~45%) which requires activation for efflorescing particles (Tang et al., 1977). If droplets encounter colder temperatures and/or higher RH$_w$, homogeneous freezing is triggered (purple trajectory 4) and ice particles can be detected. At sufficiently low temperatures deposition nucleation can occur when ice saturation is reached before the DRH (black trajectory 5) (Wise et al., 2012; Schill and Tolbert, 2014; Ladino et al., 2016). In summary, below the intersection of the ice saturation curve and the DRH line at ~245 K, three phases (anhydrous NaCl, droplets, ice) can be studied in a typical CFDC system. The di-

Table 1. Experimental onset temperature ranges for the four salts/salt solutions.

	Temperature					
	Lowest	Highest	Lowest	Highest	Lowest	Highest
	Deliquescence		Homogeneous freezing		Deposition nucleation	
NaCl	216	242	215	233	221	225
MgCl$_2$	–	–	229	233	–	–
SSW	234	237	232	233	–	–
SW	232	238	230	232	–	–

hydrate of NaCl, also thermodynamically stable in the shaded regime, exists in this regime but is beyond the scope of this work.

In this paper, we present an exploration of the NaCl system using a low-temperature CFDC, which allows us to study phase changes under conditions of atmospheric interests and also illustrates the potential application of the CFDC in detecting various phase changes in the ambient atmosphere.

2. Experiments

2.1. *Materials and sample preparation*

Four types of sea salts were used in this study: NaCl (purity > 99%, 7647-14-5, Macron Chemicals), MgCl$_2$ (purity > 98%, MFCD00011106, VWR), synthetic sea water (SSW, Paragon Scientific Limited) and natural sea water (SW, 0.45 μm filtered sea water sampled from Revere Beach, Boston, MA). The NaCl and MgCl$_2$ were dissolved in MilliQ water to produce solutions of 0.44 and 0.05 M, respectively, which represent their concentrations in real sea water. The SSW and SW were maintained in aqueous form. From the stock solutions, droplets were generated by an atomizer (Model 3076; TSI Inc., Shoreview, MN). MgCl$_2$ remains aqueous throughout experiments, while SSW and SW particles might have brine surface coatings before deliquescence (Cziczo et al., 1997). The experimentally measured onset conditions for each of the four salts, with regard to deliquescence and nucleation are listed in Table 1. The deliquescence of each of the salts, except for MgCl$_2$, was detectable using the described system. The solution droplets resulting from all four salts showed similar behaviour as HFNs, while only NaCl particles were tested for deposition nucleation in the low-temperature operation mode of SPIN (described in Section 2.2). The generated particles passed through a 43 centimetre-long dehumidifying tube at a flow rate of 0.2 L min^{-1} and mixed with dry air in an eight-litre mixing volume, resulting in a final RH$_w$ of ~15%. The resulting dried sea salt particles were size selected (mobility size ≈ 700 nm) by a differential mobility analyzer (DMA, Model 2002; Brechtel Manufacturing Inc., Hayward, CA), and flowed through a flow splitter, to a mixing condensation particle counter (CPC, Model 1700;

Brechtel Manufacturing Inc., Hayward, CA) and to the inlet of the CFDC. The CPC branch of the flow was utilised to monitor the particle number concentration. The salt particle mobility size 700 nm was selected to be representative of natural sea salt particles (O'Dowd et al., 2004; DeMott et al., 2016) and was suitable for the size differentiation of deliquescing particles by an optical particle counter (OPC) as shown in Section 3.2. Particles of such size are also large enough to ignore the influence of the Kelvin effect on the DRH (Hämeri et al., 2001; Biskos et al., 2006).

2.2. *SPIN*

Conditions at the onset of deliquescence and nucleation were determined using the SPectrometer for Ice Nuclei (SPIN; Droplet Measurement Technologies, Boulder, CO), a CFDC style instrument (Garimella et al., 2016). The upper chamber of SPIN consists of two vertically mounted, flat parallel plates whose temperatures are controlled independently. The walls are separated by a one centimetre gap and are each coated with approximately one millimetre of ice prior to experiments. Aerosol particles are constrained within a sample lamina flow of approximately 1.0 SLPM surrounded by a particle-free sheath flow of 9.0 SLPM. The temperature and relative humidity conditions, to which the sample lamina is exposed, are controlled by varying the temperature gradient between the two iced walls. A typical SPIN experiment consists of raising the lamina RH$_w$ isothermally at a rate of 2% per minute. In order to achieve the low lamina temperatures for deposition nucleation, the chamber was operated in the low-temperature mode, wherein the warm wall (with a 1-stage compressor) was maintained at its lowest temperature and the cold wall (with 2-stage compressors) continued to cool. Thus the lamina temperature decreased with increasing RH$_w$.

After passing through the upper chamber, particles enter an evaporation section that is held at ice saturation. Because the equilibrium saturation vapour pressure over liquid is higher than that over ice at the same temperature, this section promotes the evaporation of liquid droplets while allowing ice to remain and grow. When the upper chamber is operated at high RH$_w$ large droplets may form, survive transiting the evaporation section and exit SPIN to be measured – a process known as droplet breakthrough.

Upon exiting SPIN, the sample flow is directed through a 20-channel optical particle counter (OPC; laser: 500 mW, 670 nm, Osela ILS-640-250-FTH-1.5MM-100uM) that is used to obtain number concentrations, size distributions and polarisation data on measured particles. Sidescatter, polarisation intensity perpendicular to the laser beam, and two channels of polarisation intensity parallel to the incident laser beam are recorded on a particle-by-particle basis. These four parameters are then used to train a machine learning (ML) algorithm, as detailed in Garimella et al. (2016). Briefly, kernel density
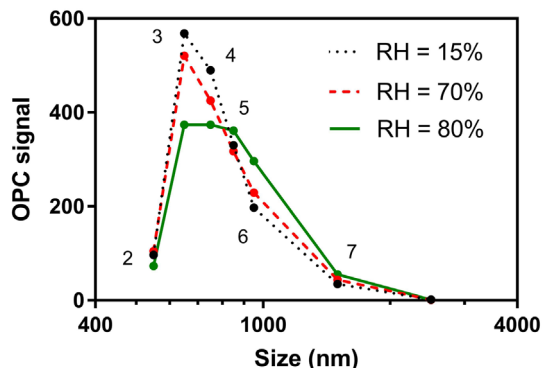
Fig. 2. NaCl size distributions at different RH$_w$ values. The lowest RH condition was obtained in a dry SPIN chamber at 293 K while the others were obtained using an ice-coated chamber with a 235 K laminar flow temperature. Notes: The numbers in the figure indicate the bin numbers.

estimation (Rosenblatt, 1956; Parzen, 1962) is used to create probability density functions (PDFs) that characterise the locations of particles in the four-dimensional parameter space discussed above. By constructing PDFs with data known to correspond to unactivated aerosol particles, water droplets and ice crystals, the ML algorithm is then able to classify an unknown particle into one of the three categories with a quantifiable classification accuracy (Mohri et al., 2012).

3.   Results and discussion

3.1.   Size distributions before and after deliquescence

Fig. 2 shows the OPC signal strength, which is proportional to the particle number concentration, plotted for the SPIN OPC size channels 2 through 7. The size distributions measured using the OPC peak around 700 nm, with a full width at half-maximum ($\approx$ 300 nm) consistent with the uncertainties of DMA size selection and the mismatch of the measurement techniques (the DMA measures mobility diameter, and the OPC an optical diameter that is affected by anisotropy). The presented distributions include, the raw DMA selection of particles exposed only to low humidities RH$_w$ $\approx$ 15% in an uniced chamber at room temperature (during the experiments, the lowest attainable RH$_w$ in the iced SPIN chamber was ~65%), those in an iced chamber at an RH$_w$ $\approx$ 70% below the DRH (235 K), and those in an iced chamber at an RH$_w$ $\approx$ 80% above the DRH (235 K). The size distribution at RH$_w$ $\approx$ 70% in the iced chamber shows a minor reduction of smaller particles accompanied by a slight enhancement of larger particles. Although this trend could indicate water uptake below the DRH (Wise et al., 2008; Alshawa et al., 2009; Bruzewicz et al., 2011; Hansen-Goos et al., 2014; Hsiao et al., 2016), it could also result from experimental uncertainties. The different wall conditions (iced versus uniced) and possible salt impurities may also lead to slight changes.
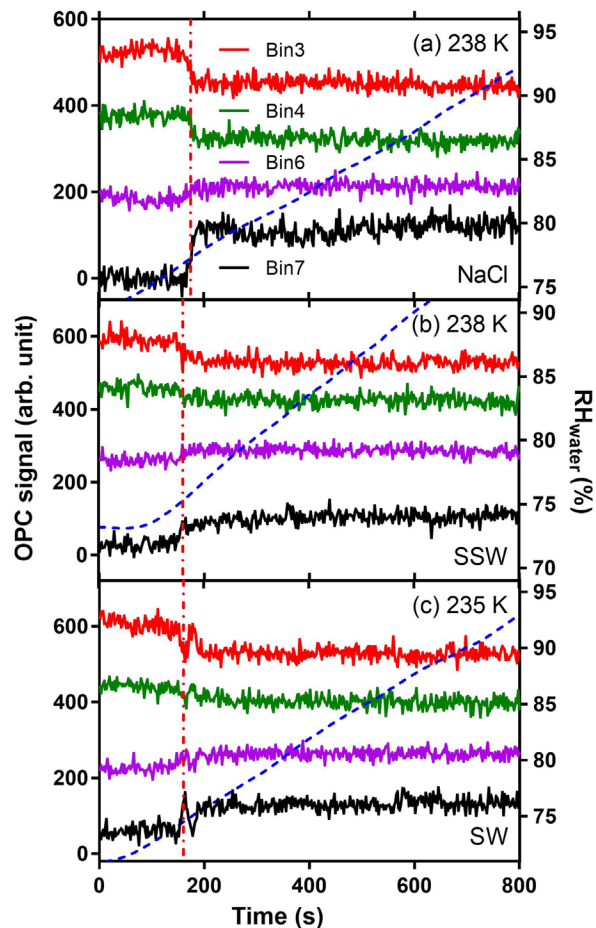

Fig. 3. The time evolution of the OPC signal of 4 size channels with three different salts corresponding to the panels. Notes: RH is plotted as a blue dashed line (right y-axis). The red dash-dotted line highlights sharp signal changes, indicating deliquescence onset. In order to separate the data for visualisation, some bin intensities were arithmetically shifted as follows: (a) bin3 + 100, bin6 -50, bin7 -600; (b) bin3 + 100, bin7 -350; (c) bin3 + 100, bin7 − 400.

More significant growth is observed due to deliquescence leading the size distribution to broaden and shift towards larger sizes (RH$_w$ $\approx$ 80%).

3.2.   Deliquescence detection

Upon deliquescence, particles larger than 100 nm in diameter rapidly grow by a factor of about two (Tang and Munkelwitz, 1993; Ming and Russell, 2001; Park et al., 2009; Hsiao et al., 2016; Morris et al., 2016; Cochran et al., 2017), which applies to the ~700 nm particles used in this study. Fig. 3 shows examples of deliquescence onset, visualised as shifts between size bin 3 (600–700 nm) and bin 4 (700–800 nm) to bin 6 (900–1000 nm) and bin 7 (1000 to 2000 nm) at the DRH for three different size-selected salts (NaCl, SSW, SW). Note that bin 7 is a wide bandwidth channel, so its absolute change as shown

in Fig. 3 is significant but much shallower in the size distribution as shown in Fig. 2 because the counts are normalised by bin width. The other bins did not show changes associated with the DRH. $MgCl_2$ deliquescence was not observed given its low DRH, around RH_w of 33% (Cziczo and Abbatt, 2000), which is below the RH_w attainable in SPIN. The onsets of the size shift are consistent with previously published DRH values (Tang and Munkelwitz, 1993; Cziczo et al., 1997; Wise et al., 2012; Wagner and Möhler, 2013; Schill and Tolbert, 2014), indicating that this quick growth corresponds to deliquescence. The ability of low-temperature CFDCs to detect solid-liquid phase change of sea salt particles at sub-water saturation (deliquescence) is only recently reported (Höhler et al., 2017; Kong et al., 2017). Because the residence time of sea salt samples in the SPIN (~10s) is short compared to traditional methods of activating particle deliquescence (Cziczo and Abbatt, 2000; Wise et al., 2012; Wagner and Möhler, 2013; Schill and Tolbert, 2014), it may be insufficient for complete deliquescence development especially at low temperature. However, this study confirms that CFDC type instruments are capable of observing deliquescence, and demonstrates that the deliquescence occurs at least within a few seconds. In the present experimental system, further droplet growth with increasing RH_w, above the DRH, is not resolved because OPC size bin 7 is a wide bandwidth channel that covers 1000 to 2000 nm sized particles (100 nm bandwidth for bin ≤ 6). Thus, it is sensitive to deliquesced droplets (700 nm × 2 = 1400 nm, shifting from bins 3 & 4 to bin 7) but less sensitive to the further gradual growth of those droplets. A gradually increasing signal in size bin 8 (2000 to 3000 nm) is not observed, implying that the observable overall growth factor is upwardly bound at $GF_{max} \approx 3$, until homogenous nucleation or droplet breakthrough occurs. Also note that, before exiting the diffusion chamber the deliquesced droplets experienced lower RH_w in the evaporation section, where the droplets may shrink back to the detection range of bin 7, even if they have grown larger.

3.3. Ice nucleation and droplet formation: detection by the OPC and phase discrimination by machine learning

As the RH_w increases beyond the DRH, deliquesced NaCl and sea salt droplets continue to grow until, either homogeneous freezing occurs or they act as CCNs above water saturation. The precise behaviour depends on temperature and RH_w as previously described. In Fig. 4, the upper panels show number concentration distributions of NaCl particles as a function of RH_w, at 231 K (left) and 237 K (right). The middle panels are snapshots of the particle size distributions at the RH_w specified by the dashed lines in the upper panels. Snapshot 1 (time 1) illustrates the unactivated NaCl particles, while snapshot 2 (time 2) shows the onset of ice nucleation (left column) or droplet breakthrough (right column). Snapshot 3 (time 3) depicts the further size evolution of activated particles at increasing RH_w.

At 231 K, ice nucleation is triggered when the RH_w corresponding to homogeneous freezing is reached, which is reflected by the sudden increase of number concentration of large particles, i.e. the broad distribution up to 6 μm at the onset of ice nucleation. Along with increasing RH_w, the ice particles keep growing and the size distribution peaks at around 10 μm at $RH_w \approx 110\%$. A fraction of smaller particles between 1 and 5 μm in diameter likely remain liquid droplets. At 237 K, ice nucleation never occurs, and the droplet size is consistent with that of the small particles at 231 K. The droplets grow with increasing RH_w, but the growth rate is not as significant as ice particles. This is expected given the SPIN design, wherein the evaporation section is used to evaporate droplets at ice saturation. The broad distribution of ice particle size is in part due to the spreading of particles outside the aerosol lamina, where the portion located in the lamina flow is about one-fourth of the total aerosol flow on average (Garimella et al., 2017). Such particle spreading outside of the lamina does not affect the accuracy of measuring the phase change onsets, because the onsets are determined by the maximum thermodynamic forcing, which is present in the lamina.

Particles are classified, with respect to phase state (anhydrous, liquid or ice) over the course of each experimental RH_w ramp, by a machine learning algorithm, based on the correlation of light scatter and polarisation data of training particles in known phases (Garimella et al., 2016). The classification accuracy for the data illustrated in Fig. 4 is 99.0% for the 231 K RH_w ramp and 99.7% for the 237 K RH_w ramp. As shown in the upper panels, ice nucleation and/or water droplet breakthrough occurs after critical RH_w are reached. In the 231 K RH_w ramp, ice particles are initially dominant, followed by an increase in water droplets after water saturation is achieved. The phases assigned by machine learning suggest that the particles are dominated by ice crystals at sizes greater than 6 μm in diameter, whereas the increase in particle counts between 2 and 6 μm in diameter, as the lamina RH_w rises above 100%, is due to droplet formation. In the 237 K RH_w ramp, ice nucleation is not observed. Droplet breakthrough is observed at an RH_w of 103% and above, and particles are on average smaller than those measured in the 237 K ramp, due to droplet evaporation within the SPIN evaporation section.

3.4. Summary of observed phase change onsets

3.4.1. Deliquescence. Fig. 5 shows the observed onsets of deliquescence (plus symbols) and ice nucleation (squares for homogeneous freezing and hexagrams for deposition nucleation) of salt particles in the NaCl–water phase diagram. The deliquescence onsets from 216 to 242 K fall along the theoretical DRH line extrapolated from higher temperature data (Tang and Munkelwitz, 1993), and agree well with previous studies that are also plotted (Wise et al., 2012; Wagner and Möhler, 2013; Schill and Tolbert, 2014). Notably, SSW
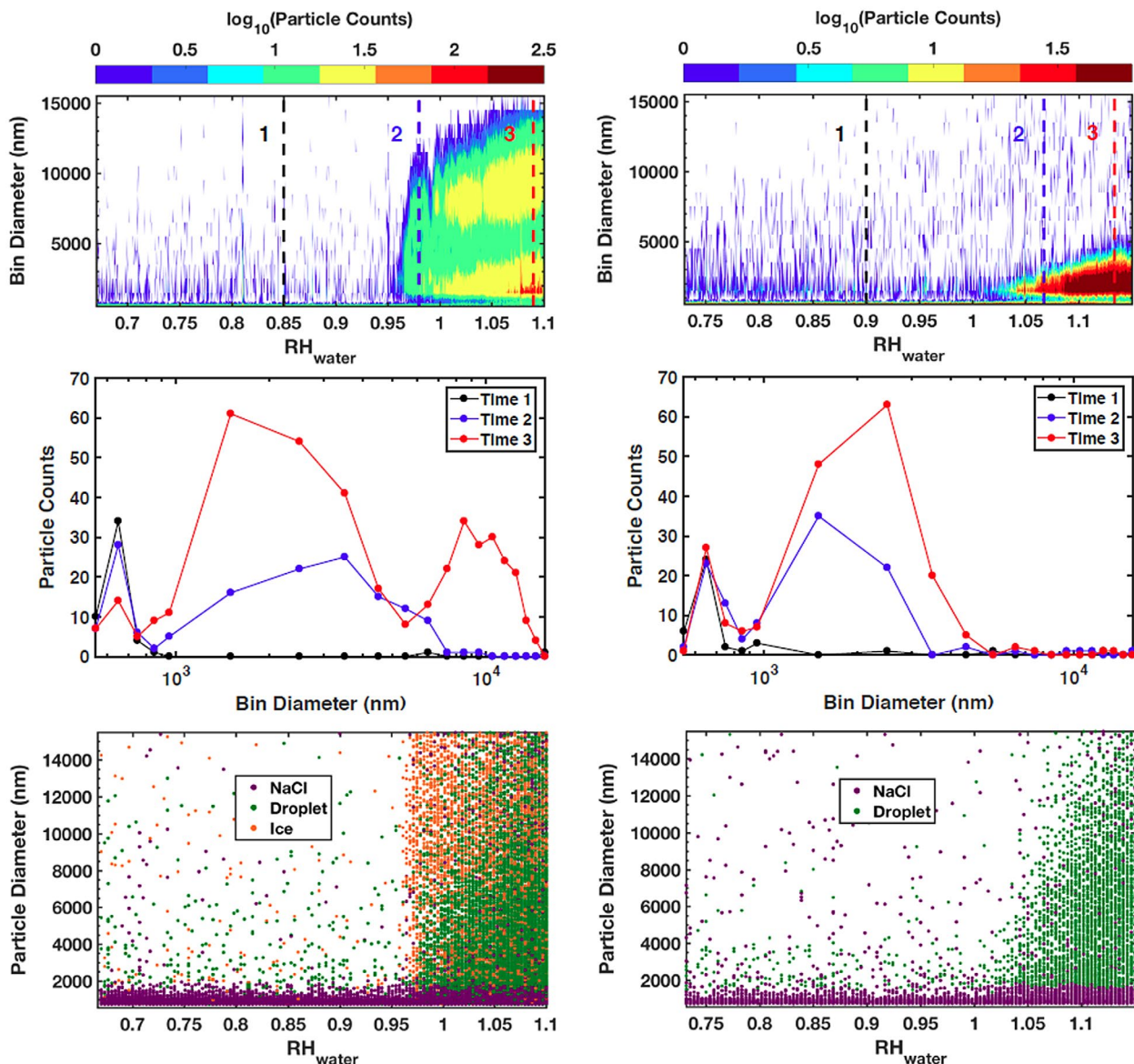
Fig. 4. Experimental NaCl particle number concentration as a function of RH$_w$ (upper panels), size distributions (middle panels) and particle composition assigned by machine learning (lower panels). Notes: The left column is observations at $T = 231$ K, while the right column corresponds to $T = 237$ K.

and SW particles (black and red pluses) deliquesce at lower DRHs than pure NaCl (blue pluses), which is likely caused by inorganic (e.g. Mg^{2+} and SO_4^{2-} salts) and organic components in the sea salt aerosol (Kester et al., 1967; Cziczo et al., 1997; O'Dowd et al., 2004; Alshawa et al., 2009; Wise et al., 2009; Schill and Tolbert, 2014; Ladino et al., 2016). The slight temperature dependence and the separation of DRH between sea salt particles of differing composition are consistent and reproducible, adding confidence in the ability of SPIN to determine DRH values at these low temperatures.

It has been shown by Wise et al. that deposition nucleation dominates deliquescence at temperatures lower than a threshold

value (~230 K) for NaCl crystals on a hydrophobic quartz plate (Wise et al., 2012). Statistically, as only a small fraction of sea salt particles act as INPs (DeMott et al., 2016), the remaining unactivated particles are expected to behave as thermodynamically predicted, that is, deliquesce at DRH. As shown in Fig.5, deliquescence of NaCl particles was observed at temperatures down to 216 K, which means that even after deposition nucleation was triggered by some salt particles at low RH$_w$, the unactivated portion deliquesced when RH$_w$ increased to DRH.

3.4.2. Ice nucleation. In Fig. 6, the critical supersaturations with respect to ice, S_i, required for deliquescence and ice nucleation
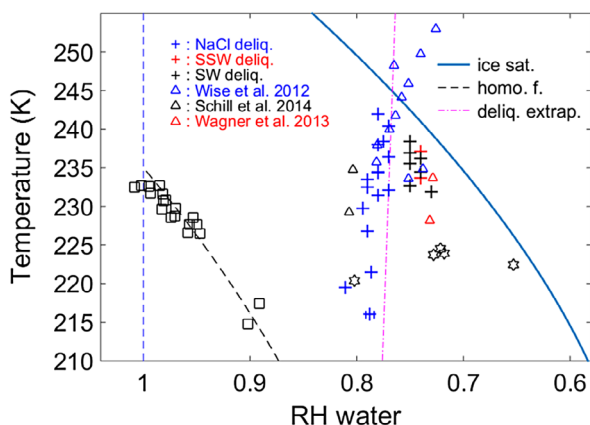
Fig. 5. Experimental data from this study in temperature/RH$_w$ space. Notes: Deliquescence (plus signs) and ice nucleation (squares and hexagrams) plotted with literature values taken from Wise et al. (2012) (blue triangles), Schill and Tolbert (2014) (black triangles), and Wagner and Möhler (2013) (red triangles). The phase boundaries are reproduced from Fig. 1. A typical error bar for deliquescence is added to the deliquescence onset RH at the lowest temperature, and the error bar is calculated as the standard deviation of the lamina temperature and relative humidity using CFD simulation code developed by Kulkarni and Kok (2012).

Fig. 6. Experimental data from the present study in ice supersaturation-temperature space. Notes: Observed deliquescence (plus symbols, same colour scheme as Fig. 5), homogenous ice nucleation (black squares) and heterogeneous nucleation (black hexagrams) are indicated. Previously published observations are taken from Schill et al. (green asterisk) (Schill and Tolbert, 2014), Wise et al. (blue triangle) (Wise et al., 2012), Wagner et al. (red triangles) (Wagner and Möhler, 2013), China et al. (green triangles) (China et al., 2017) and Ladino et al. (open circles: pure NaCl in red, Sigma-Aldrich sea salt in magenta and Instant Ocean sea salt in black) (Ladino et al., 2016). Black dots represent droplet breakthrough from this study. The phase boundaries are re-plotted from Fig. 1. The coloured shaded areas illustrate the ways in which sea salts may act as cloud seeds: CCNs in purple; CCNs/HFNs in blue; CCNs/HFNs/INPs in yellow. The error bars are calculated as the standard deviation of the lamina temperature and relative humidity using CFD simulation code developed by Kulkarni and Kok, 2012).

are shown as a function of temperature. At temperatures below 224 K, where only NaCl was tested, a fraction of the particles activate as INPs in the deposition nucleation mode and those events are shown as hexagrams. At these conditions, it is difficult to assess the competition between the kinetics of water uptake on the soluble particles versus nucleation of the thermodynamically stable ice phase. However, it is likely that these rate-dependent processes lead to the observation that approximately 15% of the total inlet particles act as INPs when DRH is reached (based on the fraction of counted ice particles versus the total amount of input particles). A similar competition between water uptake and ice nucleation on glassy organic particles has been observed (Hoose and Mohler, 2012; Berkemeier et al., 2014). This transition temperature range from deliquescence to depositional freezing agrees with previous work (Wise et al., 2012; Schill and Tolbert, 2014; Ladino et al., 2016), though the absolute critical *Si* varies in a manner that is likely due to the stochastic nature of ice nucleation and is enhanced by the different features of the experimental methods. A recent study from China et al. (2017) on free tropospheric particles shows critical *Si* that is comparable with the observations presented herein, implying sea salt strongly influences the ice nucleation activity of the particles in the air masses transported over long range and over the open ocean (Cziczo et al., 2004; Twohy and Poellot, 2005; China et al., 2017).

It is notable that the one deposition nucleation event occurs on the extrapolated DRH line (red circle), which has also been
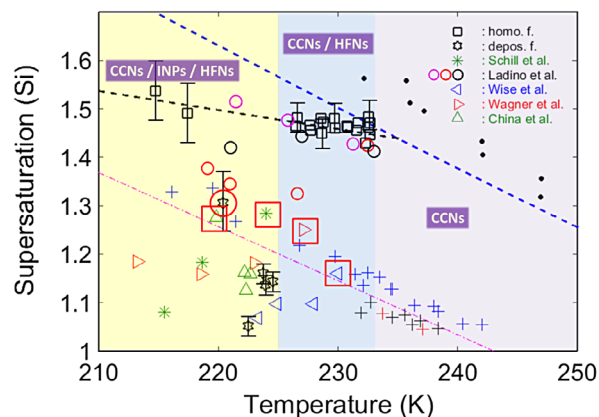
observed in previous studies (Wagner and Möhler, 2013; Schill and Tolbert, 2014; China et al., 2017) that are highlighted with red squares. Particles with mixed soluble and insoluble contents may serve as either CCNs or INPs (Khvorostyanov and Curry, 2004; Petzold et al., 2013), where the insoluble surfaces catalyse nucleation process before full deliquescence – termed as deliquescent-heterogeneous freezing (DHF). For this to occur, low temperatures are required in order that ice nucleation rates overcome deliquescence rates. At such low temperatures, the deliquesced salt solutions are supercooled and thus in a metastable equilibrium. If deliquescence is incomplete an undissolved salt core might act as a heterogeneous surface and catalyse the outer brine to freeze into the more thermodynamically favourable ice phase, i.e. the deposition nucleation here is difficult to distinguish from immersion freezing (Marcolli, 2014). This is one explanation for the overlap of critical supersaturation for ice nucleation and predicted DRH at low temperatures in this and other studies as depicted in Fig. 6.

As previously discussed, as RH$_w$ increases beyond the onset of deposition ice nucleation at low temperatures, salt particles are observed to deliquesce at DRH. This is due to the fact that deposition nucleation is observed to occur on only ~15% of the
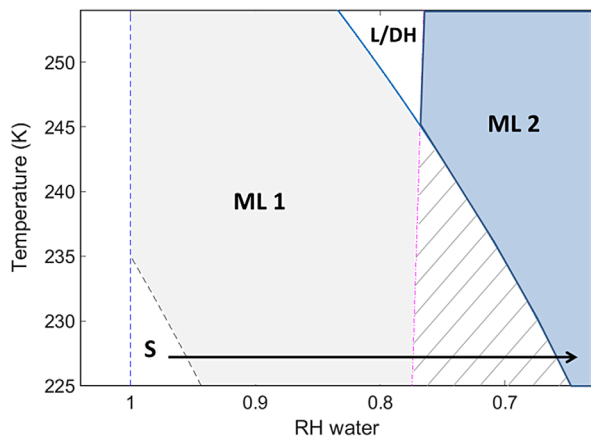
Fig. 7. NaCl water phase diagram: solid (S), supercooled metastable liquid 1 (ML1), supersaturated metastable liquid 2 (ML2), liquid (L) and dihydrate (DH).

salt particles, while the majority still deliquesce near the extrapolated DRH. Analogous behaviour for NaCl dihydrate within an intermediate range of thermodynamic phase space was reported, wherein both deposition nucleation and deliquescence of the dihydrate occurred stochastically (Wise et al., 2012).

With continuously increasing RH_w, the deliquesced solution droplets (NaCl, $MgCl_2$, SSW and SW) homogeneously freeze around the theoretical line for homogeneous freezing given by Koop et al. (2000a), assuming a nucleation rate $J \cong \sim 10^{10}$ cm^{-3} s^{-1} ($\Delta a_w = 0.305$). The observed nucleation is in excellent agreement with the extrapolation from other homogeneous freezing points at higher temperatures. Because the four types of salts show similar HFN behaviour, they are all shown as black squares to simplify the figure. In addition, the black dots in Fig. 6 indicate droplet breakthrough, where the deliquesced droplets were activated as CCNs but not INPs or HFNs at temperatures above 233 K. Thus, the salt particles show three distinct behaviours and one zone where fluctuations in the thermodynamic driving force appear to control the outcome: (1) as CCNs at >233 K (all four salts); (2) as CCNs or HFNs for homogenous nucleation between 233 K and 224 K (all four salts); (3) as CCNS, or HFNs, or INPs for heterogeneous nucleation at <224 K (only NaCl was tested).

4.   Importance of metastable liquid

In the NaCl–water phase diagram, regions exist where two types of metastable liquids overlap. Fig. 7 gives a simplified graphical representation of key regions where different phase transformation may take place. Metastable liquid 1 (ML1) is supercooled subsaturated NaCl solution, which can be formed by deliquescence or by cooling the stable solution. Notably,

in this study the transition from supercooled solution to solid phases is not observed until the temperatures get below 233 K, which is well below the eutectic point (~252 K). Metastable liquid 2 (ML2) is a supersaturated NaCl solution. Therefore, for the metastable liquid in the hashed region there are *two* thermodynamically stable solid phases, where either heterogeneous ice or salt nucleation could occur. Another uniqueness of this region is that several phases of NaCl–water combination can be found, which are (1) liquid solution (supersaturated solution, from >DRH), (2) ice + dihydrate (homogeneously frozen), (3) anhydrous NaCl (inactivated, never > DRH), (4) dihydrate (Na-Cl·$2H_2O$, marked as DH in Fig. 7) (Wagner et al., 2012; Wise et al., 2012; Peckhaus et al., 2016) and (5) ice + anhydrous NaCl (depositional freezing on NaCl particles).

More explorations of this low-temperature region of the phase space are needed, because extrapolations of higher temperature phase boundaries might yield conflicting information. Take, for example, a trajectory following the black solid arrow in Fig. 7 starting at a homogeneously frozen NaCl–ice particle that experiences an isothermal decrease in RH_w until ice subsaturation is reached. Which phase trajectory (between ice saturation and efflorescence) should it follow? Note that ice sublimation occurs at RH_w > ERH and thus, a mixture of ice and NaCl crystals can be dried more easily than a NaCl solution. If one frozen particle made of a mixture of interlacing ice and NaCl crystals (Hudait and Molinero, 2014) sublimates, then this may break down to smaller salt particles or form porous structured particles (Adler et al., 2013). Such a hypothetical process may be a multiplication mechanism for salt particles in cold ambient environments, which could be a source of sea salt in air, in addition to blowing snow, which is known to be important for airborne halogen concentrations (Yang et al., 2008; Yang et al., 2010; Huang and Jaegle, 2017). Another scenario is that NaCl and water form NaCl dihydrate, a molecularly bonded solid. In this case, NaCl dihydrate should be stable at low RH_w (< ERH), but this sublimation threshold at such low temperatures is not yet well known. The temperature range, where two MLs overlap in the phase diagram, is relevant to near surface environments of polar regions and parts of the stratosphere.

5.   Conclusions

We have demonstrated that SPIN can be used to observe sea salt and NaCl deliquescence, in addition to homogenous and heterogeneous ice nucleation. This demonstrates that the phase change upon deliquescence is detectable in the relative short residence time within the CDFC. Deliquescence of NaCl, synthesised sea salt and sampled sea water salt particles all occur at DRHs in agreement with previous studies. Synthesised sea salt and sampled sea water salt particles deliquesce at lower RH_w compared to pure NaCl, likely due to the presence of impurity

components. All four deliquesced salt solutions homogenously freeze as RH_w increases at predicted values, for temperatures below 233 K, but only act as CCNs above 233 K where droplet breakthrough was detected. Deposition nucleation occurred directly on a ~15% of NaCl particles below 224 K while those that did not act as INPs instead deliquesced and homogeneously froze as predicted. Thus, sea salt particles showed three distinct behaviours: activation as (1) CCNs at temperatures higher than 233 K; (2) CCNs or HFNs for homogenous nucleation of solution droplets from 233 K to at least 215 K; (3) CCNs, or HFNs, or INPs for heterogeneous nucleation at 224 K and lower temperatures. This study illuminates the multiple roles of atmospheric sea salt particles acting as cloud nuclei, where multiphase aerosol mixtures can be formed simultaneously from single-component salt particles.

Acknowledgements

Disclosure statement

The authors declare no conflict of interest.

Funding

References

Abbatt, J. P. D., Thomas, J. L., Abrahamsson, K., Boxe, C., Granfors, A. and co-authors. 2012. Halogen activation via interactions with environmental ice and snow in the polar lower troposphere and other regions. *Atmos. Chem. Phys.* **12**, 6237–6271.

Adler, G., Koop, T., Haspel, C., Taraniuk, I., Moise, T. and co-authors. 2013. Formation of highly porous aerosol particles by atmospheric freeze-drying in ice clouds. *P. Natl. Acad. Sci. USA* **110**, 20414–20419.

Alpert, P. A., Aller, J. Y. and Knopf, D. A. 2011. Ice nucleation from aqueous NaCl droplets with and without marine diatoms. *Atmos. Chem. Phys.* **11**, 5539–5555.

Alshawa, A., Dopfer, O., Harmon, C. W., Nizkorodov, S. A. and Underwood, J. S. 2009. Hygroscopic growth and deliquescence of NaCl nanoparticles coated with surfactant AOT. *J. Phys. Chem. A* **113**, 7678–7686.

Berkemeier, T., Shiraiwa, M., Pöschl, U. and Koop, T. 2014. Competition between water uptake and ice nucleation by glassy organic aerosol particles. *Atmos. Chem. Phys.* **14**, 12513–12531.

Biskos, G., Malinowski, A., Russell, L. M., Buseck, P. R. and Martin, S. T. 2006. Nanosize effect on the deliquescence and the efflorescence of sodium chloride particles. *Aerosol Sci. Tech.* **40**, 97–106.

Bruzewicz, D. A., Checco, A., Ocko, B. M., Lewis, E. R., McGraw, R. L. and co-authors. 2011. Reversible uptake of water on NaCl nanoparticles at relative humidity below deliquescence point observed by noncontact environmental atomic force microscopy. *J. Chem. Phys.* **134**, 044702.

China, S., Alpert, P. A., Zhang, B., Schum, S., Dzepina, K. and co-authors. 2017. Ice cloud formation potential by free tropospheric particles from long-range transport over the Northern Atlantic Ocean. *J. Geophys. Res.-Atmos.* **122**, 3065–3079.

Cochran, R. E., Laskina, O., Trueblood, J. V., Estillore, A. D., Morris, H. S. and co-authors. 2017. molecular diversity of sea spray aerosol particles: impact of ocean biology on particle composition and hygroscopicity. *Chem* **2**, 655–667.

Cziczo, D. J., Nowak, J. B., Hu, J. H. and Abbatt, J. P. D. 1997. Infrared spectroscopy of model tropospheric aerosols as a function of relative humidity: observation of deliquescence and crystallization. *J. Geophys. Res.-Atmos.* **102**, 18843–18850.

Cziczo, D. J. and Abbatt, J. P. D. 2000. Infrared observations of the response of NaCl, MgCl2, NH4HSO4, and NH4NO3 aerosols to changes in relative humidity from 298 to 238 K. *J. Phys. Chem. A* **104**, 2038–2047.

Cziczo, D. J., Murphy, D. M., Hudson, P. K. and Thomson, D. S. 2004. Single particle measurements of the chemical composition of cirrus ice residue during CRYSTAL-FACE. *J. Geophys. Res.-Atmos.* **109**, D04201.

Cziczo, D. J., Froyd, K. D., Hoose, C., Jensen, E. J., Diao, M. and co-authors. 2013. Clarifying the dominant sources and mechanisms of cirrus cloud formation. *Science* **340**, 1320–1324.

DeMott, P. J., Hill, T. C. J., McCluskey, C. S., Prather, K. A., Collins, D. B. and co-authors. 2016. Sea spray aerosol as a unique source of ice nucleating particles. *P. Natl. Acad. Sci. USA* **113**, 5797–5803.

Domine, F., Sparapani, R., Ianniello, A. and Beine, H. J. 2004. The origin of sea salt in snow on Arctic sea ice and in coastal regions. *Atmos. Chem. Phys.* **4**, 2259–2271.

Gantt, B. and Meskhidze, N. 2013. The physical and chemical characteristics of marine primary organic aerosol: a review. *Atmos. Chem. Phys.* **13**, 3979–3996.

Garimella, S., Kristensen, T. B., Ignatius, K., Welti, A., Voigtländer, J. and co-authors. 2016. The SPectrometer for Ice Nuclei (SPIN): an instrument to investigate ice nucleation. *Atmos. Meas. Tech.* **9**, 2781–2795.

Garimella, S., Rothenberg, D. A., Wolf, M. J., David, R. O., Kanji, Z. A. and co-authors. 2017. Uncertainty in counting ice nucleating particles with continuous diffusion flow chambers. *Atmos. Chem. Phys. Discuss.* **2017**, 1–28.

Hämeri, K., Laaksonen, A., Väkevä, M. and Suni, T. 2001. Hygroscopic growth of ultrafine sodium chloride particles. *J. Geophys. Res.-Atmos.* **106**, 20749–20757.

Hansen-Goos, H., Thomson, E. S. and Wettlaufer, J. S. 2014. On the edge of habitability and the extremes of liquidity. *Planet Space Sci.* **98**, 169–181.

Höhler, K., Bierbauer, S., Schiebel, T., Wagner, R. and Moehler, O. 2017. Phase change behavoir of salt aerosol in a CFDC. In: *Proceedings of the 20th International Conference on Nucleation and Atmospheric Aerosols*, Helsinki.

Hoose, C. and Mohler, O. 2012. Heterogeneous ice nucleation on atmospheric aerosols: a review of results from laboratory experiments. *Atmos. Chem. Phys.* **12**, 9817–9854.

Hsiao, T.-C., Young, L.-H., Tai, Y.-C. and Chen, K.-C. 2016. Aqueous film formation on irregularly shaped inorganic nanoparticles before deliquescence, as revealed by a hygroscopic differential mobility analyzer–Aerosol particle mass system. *Aerosol. Sci. Tech.* **50**, 568–577.

Huang, J. and Jaegle, L. 2017. Wintertime enhancements of sea salt aerosol in polar regions consistent with a sea ice source from blowing snow. *Atmos. Chem. Phys.* **17**, 3699–3712.

Hudait, A. and Molinero, V. 2014. Ice crystallization in ultrafine water–salt aerosols: nucleation, ice-solution equilibrium, and internal structure. *J. Am. Chem. Soc.* **136**, 8081–8093.

Hussain, K. and Saunders, C. P. R. 1984. Ice nucleus measurement with a continuous flow chamber. *Q. J. Roy. Meteor. Soc.* **110**, 75–84.

Johari, G. P., Fleissner, G., Hallbrucker, A. and Mayer, E. 1994. Thermodynamic continuity between glassy and normal water. *J. Phys. Chem.* **98**, 4719–4725.

Kester, D. R., Duedall, I. W., Connors, D. N. and Pytkowicz, R. M. 1967. Preparation of artificial seawater. *Limnol. Oceanogr.* **12**, 176–179.

Khvorostyanov, V. I. and Curry, J. A. 2004. The theory of ice nucleation by heterogeneous freezing of deliquescent mixed CCN. Part I: critical radius, energy, and nucleation rate. *J. Atmos. Sci.* **61**, 2676–2691.

Kong, X., Wolf, M., Garimella, S., Roesch, M. and Cziczo, D. 2017. A contineous flow diffusion chamber study of sea salt particles acting as cloud seeds:deliquescence; ice nucleation and sublimation. In: *Proceedings of the the 20th International Conference on Nucleation and Atmospheric Aerosols*, Helsinki, Finland.

Koop, T., Kapilashrami, A., Molina, L. T. and Molina, M. J. 2000a. Phase transitions of sea-salt/water mixtures at low temperatures: Implications for ozone chemistry in the polar marine boundary layer. *J. Geophys. Res.-Atmos.* **105**, 26393–26402.

Koop, T., Luo, B. P., Tsias, A. and Peter, T. 2000b. Water activity as the determinant for homogeneous ice nucleation in aqueous solutions. *Nature* **406**, 611–614.

Křepelová, A., Huthwelker, T., Bluhm, H. and Ammann, M. 2010. Surface chemical properties of eutectic and frozen NaCl Solutions probed by XPS and NEXAFS. *ChemPhysChem* **11**, 3859–3866.

Kulkarni, G. and Kok, G. 2012. *Mobile ice Nucleus Spectrometer* Pacific Northwest National Laboratory, Richland, WA.

Ladino, L. A., Yakobi-Hancock, J. D., Kilthau, W. P., Mason, R. H., Si, M. and co-authors. 2016. Addressing the ice nucleating abilities of marine aerosol: a combination of deposition mode laboratory and field measurements. *Atmos. Environ.* **132**, 1–10.

Marcolli, C. 2014. Deposition nucleation viewed as homogeneous or immersion freezing in pores and cavities. *Atmos. Chem. Phys.* **14**, 2071–2104.

Martin, S. T. 2000. Phase transitions of aqueous atmospheric particles. *Chem. Rev.* **100**, 3403–3454.

Ming, Y. and Russell, L. M. 2001. Predicted hygroscopic growth of sea salt aerosol. *J. Geophys. Res.-Atmos.* **106**, 28259–28274.

Mohri, M., Rostamizadeh, A. and Talwalkar, A. 2012. *Foundations of Machine Learning* MIT Press, Cambridge, MA.

Morris, H. S., Estillore, A. D., Laskina, O., Grassian, V. H. and Tivanski, A. V. 2016. Quantifying the hygroscopic growth of individual submicrometer particles with atomic force microscopy. *Anal. Chem.* **88**, 3647–3654.

O'Dowd, C. D., Smith, M. H., Consterdine, I. E. and Lowe, J. A. 1997. Marine aerosol, sea-salt, and the marine sulphur cycle: a short review. *Atmos. Environ.* **31**, 73–80.

O'Dowd, C. D., Facchini, M. C., Cavalli, F., Ceburnis, D., Mircea, M. and co-authors. 2004. Biogenically driven organic contribution to marine aerosol. *Nature* **431**, 676–680.

Park, K., Kim, J.-S. and Miller, A. L. 2009. A study on effects of size and structure on hygroscopicity of nanoparticles using a tandem differential mobility analyzer and TEM. *J. Nanopart. Res.* **11**, 175–183.

Parzen, E. 1962. On estimation of a probability density function and mode. *Ann. Math. Statist.* **33**, 1065–1076.

Peckhaus, A., Kiselev, A., Wagner, R., Duft, D. and Leisner, T. 2016. Temperature-dependent formation of NaCl dihydrate in levitated NaCl and sea salt aerosol particles. *J. Chem. Phys.* **145**, 12.

Petzold, A., Formenti, P., Baumgardner, D., Bundke, U., Coe, H. and co-authors 2013. In situ measurements of aerosol particles. In: *Airborne Measurements for Environmental Research*. Wiley-VCH Verlag GmbH & KGaA, pp. 157–223.

Rogers, D. C. 1988. Development of a continuous flow thermal gradient diffusion chamber for ice nucleation studies. *Atmos. Res.* **22**, 149–181.

Rosenblatt, M. 1956. Remarks on some nonparametric estimates of a density function. *Ann. Math. Statist.* **27**, 832–837.

Schill, G. P. and Tolbert, M. A. 2014. Heterogeneous ice nucleation on simulated sea-spray aerosol using raman microscopy. *J. Phys. Chem. C* **118**, 29234–29241.

Tang, I. N., Munkelwitz, H. R. and Davis, J. G. 1977. Aerosol growth studies—II. Preparation and growth measurements of monodisperse salt aerosols. *J. Aerosol Sci.* **8**, 149–159.

Tang, I. N. and Munkelwitz, H. R. 1993. Composition and temperature dependence of the deliquescence properties of hygroscopic aerosols. *Atmos. Environ. Part A. General Topics* **27**, 467–473.

Twohy, C. H. and Poellot, M. R. 2005. Chemical characteristics of ice residual nuclei in anvil cirrus clouds: evidence for homogeneous and heterogeneous ice formation. *Atmos. Chem. Phys.* **5**, 2289–2297.

Wagner, R., Möhler, O. and Schnaiter, M. 2012. Infrared optical constants of crystalline sodium chloride dihydrate: application to study the crystallization of aqueous sodium chloride solution droplets at low temperatures. *J. Phys. Chem. A* **116**, 8557–8571.

Wagner, R. and Möhler, O. 2013. Heterogeneous ice nucleation ability of crystalline sodium chloride dihydrate particles. *J. Geophys. Res.-Atmos.* **118**, 4610–4622.

Wise, M. E., Martin, S. T., Russell, L. M. and Buseck, P. R. 2008. Water uptake by nacl particles prior to deliquescence and the phase rule. *Aerosol Sci. Tech.* **42**, 281–294.

Wise, M. E., Freney, E. J., Tyree, C. A., Allen, J. O., Martin, S. T. and co-authors. 2009. Hygroscopic behavior and liquid-layer composition of aerosol particles generated from natural and artificial seawater. *J. Geophys. Res.-Atmos.* **114**, 8.

Wise, M. E., Baustian, K. J., Koop, T., Freedman, M. A., Jensen, E. J. and co-authors. 2012. Depositional ice nucleation onto crystalline hydrated NaCl particles: a new mechanism for ice formation in the troposphere. *Atmos. Chem. Phys.* **12**, 1121–1134.

Yang, X., Pyle, J. A. and Cox, R. A. 2008. Sea salt aerosol production and bromine release: role of snow on sea ice. *Geophys. Res. Lett.* **35**, D16105.

Yang, X., Pyle, J. A., Cox, R. A., Theys, N. and Van Roozendael, M. 2010. Snow-sourced bromine and its implications for polar tropospheric ozone. *Atmos. Chem. Phys.* **10**, 7763–7773.

Yang, X., Neděla, V., Runštuk, J., Ondrušková, G., Krausko and co-authors. 2017. Evaporating brine from frost flowers with electron microscopy and implications for atmospheric chemistry and sea-salt aerosol formation. *Atmos. Chem. Phys.* **17**, 6291–6303.